Check for updates

View Article Online
View Journal

Chemical Science

Accepted Manuscript

This article can be cited before page numbers have been issued, to do this please use: D. He, J. L. Cabrelles, J. D. Evans and S. Furukawa, *Chem. Sci.*, 2026, DOI: 10.1039/D6SC03012B.

This is an Accepted Manuscript, which has been through the Royal Society of Chemistry peer review process and has been accepted for publication.

Accepted Manuscripts are published online shortly after acceptance, before technical editing, formatting and proof reading. Using this free service, authors can make their results available to the community, in citable form, before we publish the edited article. We will replace this Accepted Manuscript with the edited and formatted Advance Article as soon as it is available.

You can find more information about Accepted Manuscripts in the Information for Authors.

Please note that technical editing may introduce minor changes to the text and/or graphics, which may alter content. The journal's standard Terms & Conditions and the Ethical guidelines still apply. In no event shall the Royal Society of Chemistry be held responsible for any errors or omissions in this Accepted Manuscript or any consequences arising from the use of any information it contains.

ROYAL SOCIETY OF CHEMISTRY

rsc.li/chemical-science

Please do not adjust margins

View Article Online
DOI: 10.1039/D6SC03012B

ARTICLE

Phase-Dependent Responsiveness in Soft Porous Crystals Assembled from Flexible Metal–Organic Cages

Donglin He,*[a] Javier López Cabrelles,[a] Jack D. Evans [b] and Shuhei Furukawa *[a, c]

Received 00th January 20xx,
Accepted 00th January 20xx

DOI: 10.1039/x0xx00000x

Soft porous crystals (SPCs) based on flexible metal–organic cages (MOCs) remain elusive due to challenges in preserving both dynamic behavior and crystallinity after desolvation. Here, we report an SPC assembled from flexible metal–organic cages (MOCs), in which the resulting porous properties, either conventional microporous filling or gate-opening behavior, depend on the activation process. The flexible MOCs are constructed by a covalent linking strategy; amine-functionalized dirhodium paddlewheel complexes serve as building blocks and are connected with aldehyde units through Schiff base condensation. By systematically tuning ligand substituents, axial pyridine coordination, and activation conditions, we achieve a delicate balance between crystallinity and flexibility. Notably, one compound provided two distinct activated phases under different activation conditions. Their structures were determined by three-dimensional electron diffraction (3D ED). One phase displays a conventional type I CO_2 isotherm at 195 K, confirming the rigid MOC assembly. In contrast, the other phase exhibits reversible stepwise CO_2 adsorption accompanied by hinge-like ligand flipping and packing rearrangements, as confirmed by *in situ* powder X-ray diffraction (PXRD) and atomistic simulations. In this system, the gas-responsive behavior is governed by both molecular conformation and packing, providing a unique strategy for developing a novel SPC class based on the flexible MOCs.

Introduction

The concept of soft porous crystals (SPCs) originates from metal-organic frameworks (MOFs), which exhibit reversible channel modulation responding to external stimuli while maintaining crystallinity.[1-3] This unique combination of 'softness' and 'regularity' opens new avenues for designing functional materials with adaptive porous properties, such as selective gas adsorption,[4] and separation[5]. The success of MOFs as SPCs lies in their extended networks, in which strong covalent and coordination bonds facilitate cooperative structural dynamics, particularly in response to gas sorption.[6-10]

Metal-organic cages (MOCs), the molecular counterparts of MOFs, are discrete metal complexes with accessible and tunable cavities.[11,12] Their solubility has enabled extensive investigations into their structural dynamics in solution, revealing that flexible MOCs undergo diverse conformational motions such as ligand isomerization,[13] flipping,[14] rotation,[15] and breathing[16] driven by the intrinsic flexibility of their organic components. Thus, MOCs hold promise for constructing SPCs; however, there are only a few examples due to the challenge of retaining both crystallinity and flexibility in the solid state.[17,18] The reasons for such difficulties can be explained as follows. First, the solvent-removal process, known as activation, often leads to structural collapse or loss of crystallinity due to weak intermolecular interactions between discrete MOC molecules.[19-21] As a result, it is difficult to determine the activated structure by single-crystal X-ray diffraction (SC-XRD). Second, unlike MOFs, MOCs often crystallize in low-symmetry space groups, which makes it challenging to refine the activated structure by powder X-ray diffraction (PXRD). Third, even if crystallinity is retained and the ligands are flexible, the limited molecular mobility and rigid packing in the solid state typically restrict dynamic structural responses.

Here we present a series of lantern-type Rh-based MOCs (RhMOCs) with flexible imine moieties that exhibit flipping conformational motion. As illustrated in Figure 1, the discrete flexible MOCs are assembled into crystalline solids, which retain their crystallinity upon solvent removal. One of the compounds shows two distinct activated phases, depending on the activation methods. Three-dimensional electron diffraction (3D ED) allows us to solve both structures: one phase with MOCs in a flipped conformation and the other in a straight conformation. While the former shows a Type I gas adsorption isotherm, the latter demonstrates a stepwise adsorption isotherm. In situ PXRD experiments under controlled gas pressure and computational simulations reveal that stepwise adsorption

[a] Institute for Integrated Cell-Material Sciences (WPI-iCeMS), Kyoto University, Yoshida, Sakyo-ku, Kyoto 606-8501, Japan. Email: shuhei.furukawa@icems.kyoto-u.ac.jp
[b] School of Physics, Chemistry and Earth Sciences, The University of Adelaide, North Terrace, Adelaide 5005, South Australia, Australia
[c] Department of Synthetic Chemistry and Biological Chemistry, Graduate School of Engineering, Kyoto University, Katsura, Nishikyo-ku, Kyoto 615-8510, Japan

Open Access Article. Published on 24 June 2026. Downloaded on 6/25/2026 4:46:59 AM.
This article is licensed under a Creative Commons Attribution-NonCommercial 3.0 Unported Licence.

Chemical Science Accepted Manuscript

Please do not adjust margins

Open Access Article. Published on 24 June 2026. Downloaded on 6/25/2026 4:46:59 AM. This article is licensed under a Creative Commons Attribution-NonCommercial 3.0 Unported Licence.

arises from cooperative structural changes in MOCs, accompanied by the flipping motion of imine moieties. This work provides a detailed understanding of the correlation between molecular and packing dynamics in SPCs formed from flexible MOCs and offers a design strategy for responsive porous materials.

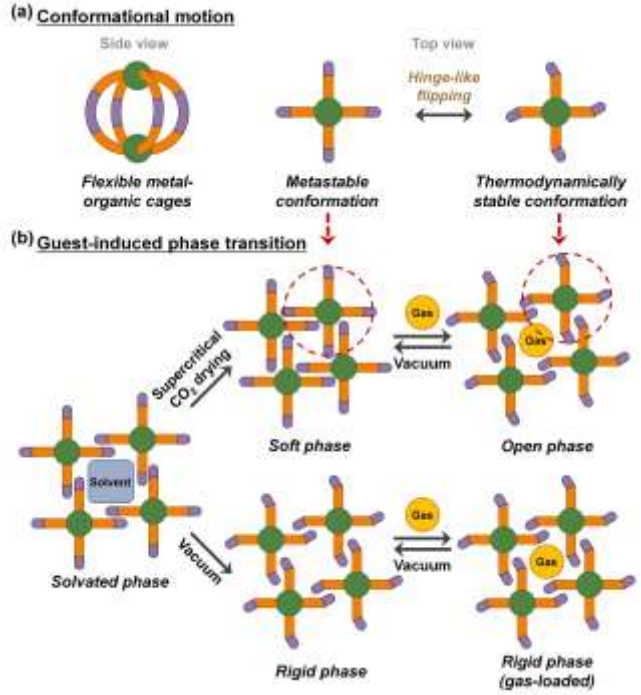

Figure 1. Conceptual scheme of conformational dynamics and phase transitions in flexible MOCs. (a) Hinge-like flipping between MOC conformations. (b) Activation-dependent phase behaviour: the soft phase exhibits reversible gate-opening, while the rigid phase remains a similar structure with gas adsorption.

Results and discussion

Synthesis and Characterization of flexible RhMOCs. Conventionally, MOCs are synthesized through the coordination assembly of metal ions/clusters and organic ligands, where coordination bonds form simultaneously during cage construction.[22] Even with carefully selected metal centres and ligands, precise control over MOC structures remains challenging, especially when using flexible ligands.[11,23] Though essential for imparting structural dynamics, the incorporation of flexible functional groups in ligand scaffolds can further complicate the self-assembly process due to their conformational freedom, leading to the disruption of binding geometries or the formation of kinetic polymeric products.

To overcome these limitations, we propose a covalent linking strategy using pre-functionalized metal clusters and organic precursors to introduce flexible moieties into MOCs (Figure 2). This strategy employs Schiff base condensation, inspired by dynamic covalent chemistry in porous organic cages, where reversible imine formation enables error-correction and the formation of thermodynamically stable structures.[24] Chemically robust dirhodium paddlewheel clusters were selected as stable building blocks for covalent functionalization.[25,26] The resulting imine moieties undergo hinge-like flipping accompanied by the rotation of the three adjacent benzene rings, thereby imparting flexibility to the MOCs (Figure 2c).

View Article Online DOI: 10.1039/D6SC03013B

The key dirhodium paddlewheel precursor, $Rh_2\{m\text{-}(NH_2)ArCO_2\}_4$ (*m*-$(NH_2)ArCO_2$ = 3-aminobenzoate), bearing four pendant amine groups, was synthesized using a Boc-protection strategy inspired by previous reports.[27,28] As shown in Figure S1–S3 (SI Sections 2.1–2.3), protection of 3-aminobenzoic acid followed by complexation with $RhCl_3$ and sodium ethoxide afforded the Boc-protected paddlewheel, which was subsequently deprotected using $HClO_4$ in methanol to yield the target complex. Structural characterization by nuclear magnetic resonance (NMR) spectroscopy, mass spectrometry (MS), and SC-XRD confirmed the successful formation of the $Rh_2\{m\text{-}(NH_2)ArCO_2\}_4$ (SI Section 2.3, Figure S9 and S18). Subsequent condensation with 2-hydroxyisophthalaldehyde derivatives (R = H, CH_3, or $C(CH_3)_3$) either at room temperature (RT) or at 65 °C afforded imine-linked lantern-type RhMOCs (SI Section 2.4-2.9). Unlike conventional RhMOC synthesis, which typically requires high temperatures ($\geqslant$ 100 °C) due to the ligand exchange reaction with the inert equatorial carboxylates of the commonly used $Rh_2(O_2CCH_3)_4$ precursor,[11, 29] this approach yielded single crystals within a few hours at RT. Time-resolved optical microscopy images of single crystal growth are shown in Figures S4–S7. The structures of all the solvated RhMOCs were confirmed by SC-XRD, and detailed structural features are discussed in the following section.

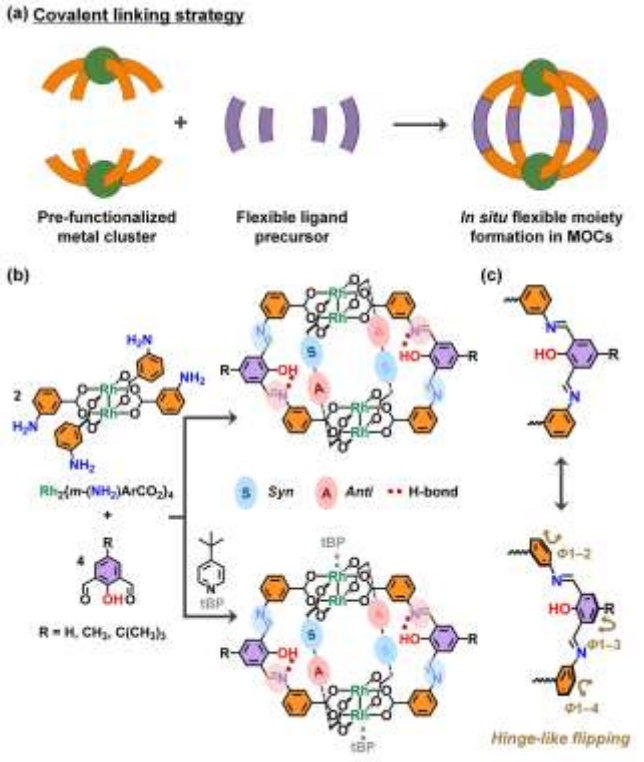

Figure 2. (a) Schematic diagram of covalent linking strategy for the synthesis of flexible MOCs. (b) Design and construction of flexible RhMOCs through *in situ* covalent linking and ligand engineering. *Syn/anti* imine conformations, stabilized by intramolecular hydrogen bonds (red dashed lines), and cis arrangements of the ligands within the RhMOC. (c) Hinge-like flipping of an imine-linked ligand arm, illustrating how rotation around the imine bond imparts dynamic flexibility at the molecular level.

Chemical Science Accepted Manuscript

This journal is © The Royal Society of Chemistry 20xx

Please do not adjust margins

View Article Online
DOI: 10.1039/D6SC03012B

Open Access Article. Published on 24 June 2026. Downloaded on 6/25/2026 4:46:59 AM.
This article is licensed under a Creative Commons Attribution-NonCommercial 3.0 Unported Licence.

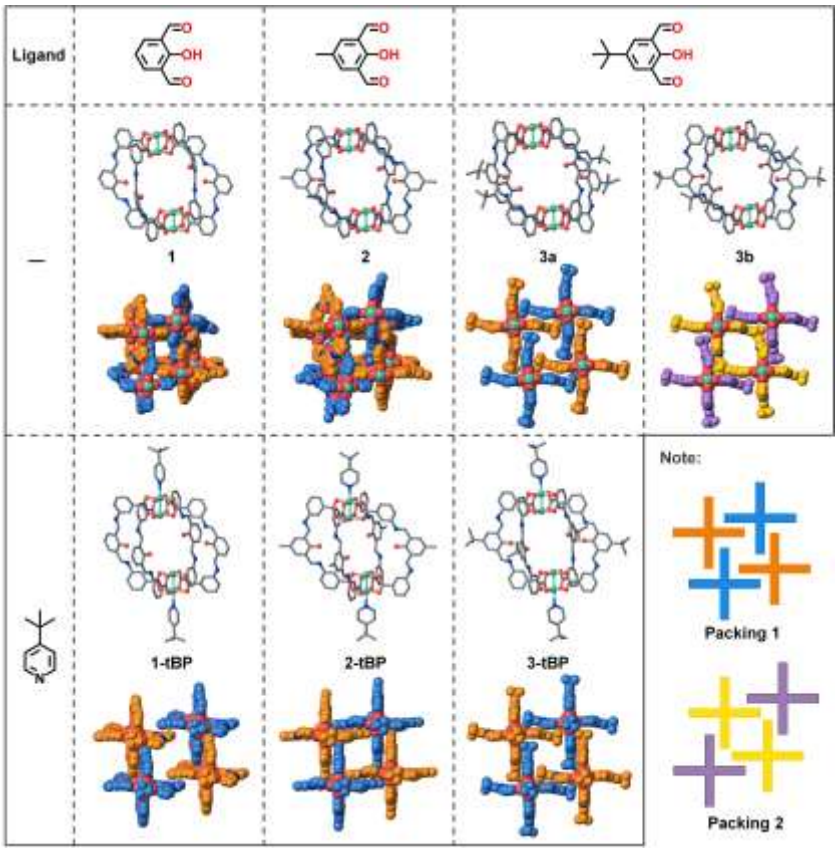

Figure 3. Single crystal structures of solvated RhMOCs and their packing arrangements. H atoms, solvent molecules, and disordered parts are omitted for clarity (green, Rh; blue, N; red, O; grey, C). Two distinct packing modes are observed: Packing 1 (orange and blue) and Packing 2 (yellow and purple).

The general formula of RhMOCs is found to be Rh_4(x-IL-OH)$_4$(solvent)$_4$, where x-IL-OH refers to 2-hydroxy-*N*,*N*′-bis(4-carboxybenzylidene)-1,3-phenylenediamine with x representing the following substituent at the 5-position: hydrogen (H), methyl (Me), or *tert*-butyl (tBu). The "solvent" refers to coordinating solvent molecules, which occupy the axial sites of the dirhodium paddlewheels (Figure 2b). For clarity, the resulting Rh_4(x-IL-OH)$_4$(solvent)$_4$ are denoted as **1** (x = H), **2** (x = Me), and **3** (x = tBu), irrespective of the coordinated solvent molecules.

To modulate intermolecular interactions between RhMOCs, we introduced a bulky ligand, 4-*tert*-butylpyridine (tBP), which selectively coordinates at the external axial sites of the dirhodium paddlewheels. The resulting complexes, with the general formula of Rh_4(x-IL-OH)$_4$(tBP)$_2$(solvent)$_2$, are referred to as **1-tBP** (x = H), **2-tBP** (x = Me), and **3-tBP** (x = tBu), regardless of the coordinating solvent (Figure 2b and 3).

The molecular composition of the bulk samples was analysed by NMR after the acid digestion, matrix-assisted laser desorption ionization-time-of-flight mass spectrometry (MALDI-TOF MS), and infrared (IR) spectroscopy. As shown in Figures S19–S24, the ^{1}H NMR spectra of the digested samples revealed that the ratio of 3-aminobenzoic acid, dialdehyde, and tBP closely matches the expected stoichiometries: (8:4:0) for compounds **1**, **2**, and **3**, and (8:4:2) for **1-tBP**, **2-tBP**, and **3-tBP**. In the MALDI-TOF MS spectra (Figures S25–S30), the molecular ion peak corresponding to the RhMOC core without the coordination of any molecules at the axial sites of the dirhodium paddlewheels was observed in all samples. The tBP molecules coordinating at the axial sites were most likely removed during ionization due to their weak binding. The presence of the imine linkages (νC=N = 1615–1700 cm^{-1}) in the solid state was confirmed through IR spectroscopy (Figures S31–S33). These results collectively confirm the successful synthesis of RhMOCs and their high purity.

Chemical Science Accepted Manuscript

Please do not adjust margins

View Article Online
DOI: 10.1039/D6SC07012F

Open Access Article. Published on 24 June 2026. Downloaded on 6/25/2026 4:46:59 AM. This article is licensed under a Creative Commons Attribution-NonCommercial 3.0 Unported Licence.

Crystal Structures of Solvated RhMOCs. The solvated crystal structures revealed that four imine ligands (x-IL-OH) bridge two dirhodium paddlewheel nodes to form the lantern-type MOC structures (Figures 2 and 3). All molecular structures exhibited a similar molecular configuration, regardless of the substituent (H, Me, or tBu) or the presence of axially coordinating tBP. As shown in Figure 2b, all four ligands in each RhMOC adopt a uniform *syn–anti* configuration[30], in which the *syn* and *anti* orientations of the imine moieties are highlighted in blue and red, respectively. Note that intramolecular O-H···N hydrogen bonds are observed between the phenolic hydroxyl groups and adjacent imine nitrogen atoms (O···N around 2.56–2.63 Å as determined from SC-XRD; red dashed lines in Figure 2b), which further stabilize this specific conformation.[31] These four ligands adopt a *cis*-arrangement, with the ligands on the diagonal reversed.

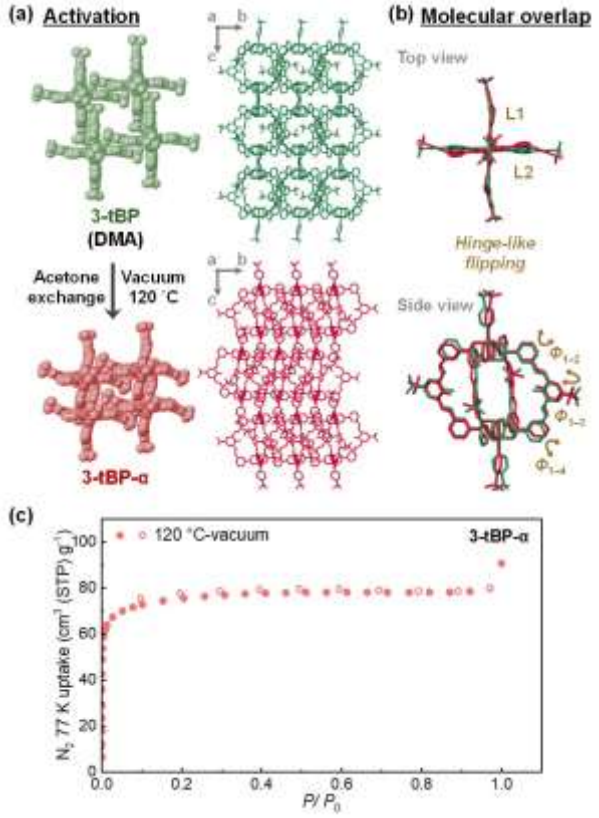

Figure 4. (a) Crystal packing of as-synthesized **3-tBP** (solvated, green) and after solvent exchange followed by vacuum activation at 120 °C (**3-tBP-α**, red) with corresponding unit-cell axes. (b) Top and side overlap of the single RhMOC from solvated **3-tBP** (green) and **3-tBP-α** (red), highlighting hinge-like flipping of the imine-linked ligand arms. (c) N_2 sorption isotherms at 77 K for **3-tBP-α** (red).

Despite the similar ligand configuration, the twisting of the imine moieties varies markedly among the RhMOCs, occurring through the rotation of the three adjacent benzene rings in a hinge-like flipping fashion (Figure 2c and 3). To quantitatively describe this flipping, four planes (*P*1–*P*4) were defined along the ligand backbone (Figure S54). *P*1 is defined by the plane passing through the carboxylate oxygen atoms bound to the dirhodium paddlewheel, while *P*2, *P*3, and *P*4 correspond to the successive benzene rings extending from the imine moieties. The degree of flipping was evaluated by calculating the dihedral angles (Φ_{1-2}, Φ_{1-3}, and Φ_{1-4}) between the normal vectors of these planes according to the equation in SI Section 15. (Figure 2c) Due to the approximate C_2 symmetry of the RhMOC, the four bridging ligands are arranged in two symmetry-equivalent pairs. Therefore, only two adjacent ligands (L1 and L2) are discussed in the following calculations. The Φ_{1-3} dihedral angle, which involves the benzene ring connected by two imine bonds, provides the most visible measure of the flipping motion from the top view and varies in the range of 4 – 38° (summarized in Table S8-S14). The two benzene rings connected to the dirhodium paddlewheel, described by Φ_{1-2} and Φ_{1-4}, also undergo independent twisting, with angle variations of 1 – 25°. Together, these three dihedral angles provide a comprehensive measure of the overall conformational motion of the RhMOC as described below.

All solvated RhMOCs exhibit layered packing arrangements, in which intralayer packing arises from intermolecular interactions between the imine ligands of adjacent RhMOCs. As shown in Figure 3, the packing modes within each layer can be classified into two types. Packing 1, observed in structures **1**, **2**, **3a**, and their tBP analogues, exhibits an interdigitated-like cross-arrangement, characterized by staggered and close contacts between the ligands of adjacent RhMOCs. The more open packing 2 is unique to **3b**, a polymorph co-produced with **3a** in the same reaction vessel. A comparison between structures with and without tBP reveals that the steric bulk of tBP slightly disrupts the tight packing within the layers.

The interlayer interactions are primarily maintained by solvent molecules or tBP coordinated at the external axial sites of the dirhodium paddlewheels (Figure S10-S16). Specifically, structures **1** and **2** exhibit similar packing arrangements, as do their tBP analogues, **1-tBP** and **2-tBP**. In both pairs, the RhMOCs stack in ordered layers with similar orientation.

Activation-Induced Structural Transformation. The removal of solvents from crystals, known as activation, often results in the loss of long-range order in MOC systems due to the collapse of solvent-stabilized packing and the inherent nature of weak inter-cage interactions. Thus, there are a few reports on the precise structural and porosity analysis of MOCs after activation.[20] To gently activate the sample, we employed the supercritical CO_2 ($ScCO_2$) drying process as follows.[32,33] The as-synthesized crystals in DMA were first exchanged with a 1:1 (v/v) mixture of DMA and acetone for 10 minutes, followed by two additional exchanges with pure acetone, each lasting 10 minutes. The resulting samples were activated by the $ScCO_2$. For comparison, a conventional activation method was also applied, in which acetone-exchanged samples were dried under vacuum at room temperature (RTV) or at 120 °C.[34]

The PXRD experiments (Figure S34-39) revealed that all samples retained crystallinity after both activation processes and exhibited structural changes. Notably, the activated RhMOCs without tBP exhibited the broadening of the diffractions compared to their tBP-containing analogues. This difference suggests that the coordinating tBP helps samples retain the crystallinity during the activation process.

Chemical Science Accepted Manuscript

 This journal is © The Royal Society of Chemistry 20xx

View Article Online
DOI: 10.1039/D5SC03913B

Open Access Article. Published on 24 June 2026. Downloaded on 6/25/2026 4:46:59 AM.
This article is licensed under a Creative Commons Attribution-NonCommercial 3.0 Unported Licence.

Particularly, the activated **2-tBP** and **3-tBP** crystals maintained high crystallinity.

By taking advantage of the preserved high crystallinity, we obtained structural information on the activation-induced transformation in **3-tBP**. Upon thermal activation at 120 °C under vacuum, single crystals of the activated phase (**3-tBP-α**) suitable for SC-XRD were obtained. The structure reveals a symmetry reduction upon activation from *C*2/*c* to $P2_1/c$, along with a 34% reduction in unit-cell volume (Figure 4a). As shown in the molecular overlay in Figure 4b and the dihedral angle data in Table S14-S15, the structure of **3-tBP-α** exhibits pronounced hinge-like flipping of all three benzene rings around the central imine linkages. Notably, Φ_{1-3} and Φ_{1-4} of ligand L2 increase significantly from 9° to 26° and from 1° to 24°, respectively. In ligand L1, Φ_{1-2} increases from 2° to 12°, while Φ_{1-4} remains unchanged (12°). These results indicate that the conformational transformation involves not only the central benzene ring (Φ_{1-3}) but also significant twisting of the outer arms (Φ_{1-2} and Φ_{1-4}).

TGA measurements indicated that thermal activation at 120 °C is effective for **3-tBP-α**, fully removing trapped solvent (Figure S48). N_2 sorption isotherms at 77 K (Figure 4c) revealed the typical type I isotherm (54 cm^3/g at P/P_0 = 0.01), with a BET surface area of 290 m^2/g calculated by BETSI v2.0 (Figure S49),[35] closely matching the theoretical surface area (288 m^2/g) calculated from its single-crystal structure by Zeo++.[36] As shown in Figure S50, the permanent porosity of **3-tBP-α** is attributed to its sufficiently large pores and channels that both exceed the kinetic diameter of N_2 (kinetic diameter, Dk = 3.64 Å) and even CO_2 (Dk = 3.30 Å). Specifically, the maximum pore diameter, defined by the largest included sphere along the free sphere path (Dif), is 5.75 Å, and the channel window diameter, defined by the largest free sphere (Df), is 4.89 Å.[36] These dimensions indicate that the crystal has the necessary porosity to allow these gases to diffuse through its structure.

By comparison, compound **3**, without the coordinated tBP, activated under vacuum at 120 °C, exhibited a relatively high N_2 uptake (~50 cm^3/g at P/P_o = 0.01) as shown in Figure S44a. Since the activated **3** appeared to be a mixture of different crystalline phases, its structure could not be reliably determined and is therefore not discussed further. Other samples after activation were also tested for N_2 sorption at 77 K and CO_2 sorption at 195 K (Figure S40-42). Activated **1**, **2**, and **1-tBP** show negligible porosity toward N_2.

Process-Dependent Activated Phases with Distinct Sorption Property. Thanks to the maintenance of high crystallinity of **2-tBP** during solvent exchange and activation, we were able to obtain crystal structures at all steps of the activation. Note that the detailed PXRD analysis further showed that two distinct activated phases of **2-tBP** were obtained depending on the activation methods: **2-tBP-α** via conventional RTV activation and **2-tBP-β** via $ScCO_2$ drying process (Figure S36a). The structure of the acetone-exchanged crystal, **2-tBP-acetone,** was determined by SC-XRD. The two distinct activated phases, **2-tBP-α** and **2-tBP-β**, were confirmed by 3D ED, an effective technique for directly observing structural transformations in MOCs.[37] As shown in Figure 5a, Table S3 and S5, all three structures retain the triclinic *P*-1 symmetry but exhibit progressive structural contraction upon solvent exchange and removal. First, the intermediate **2-tBP-acetone** structure shows a moderate unit-cell volume contraction (~14%) relative to the parent **2-tBP**. Further solvent removal induces a more distinct structural transformation. **2-tBP-α** undergoes a hinge-like

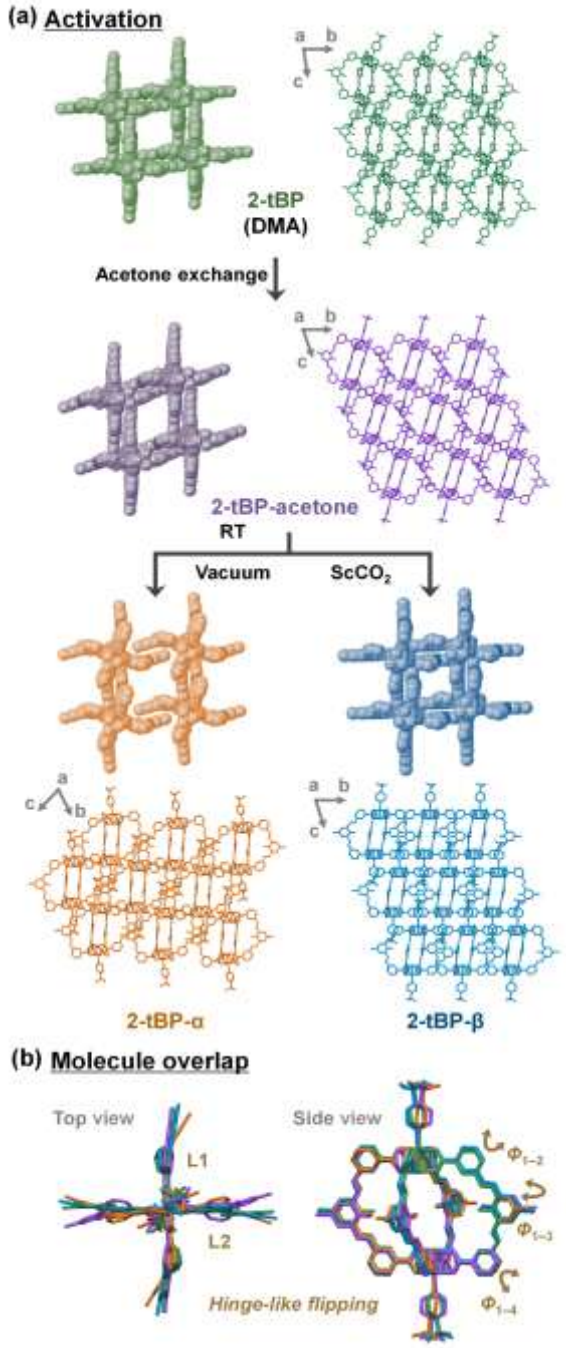

Figure 5. (a) Crystal packing of **2-tBP** in its as-synthesized (solvated, green) form, after acetone exchange (**2-tBP-acetone**) and following activation by room-temperature vacuum (**2-tBP-α**, orange) or $ScCO_2$ drying (**2-tBP-β**, blue). Unit-cell axes a, b, c are shown for each packing. (b) Top and side overlap of the single RhMOC from the solvated **2-tBP** (green), **2-tBP-acetone** (purple), **2-tBP-α** (orange) and **2-tBP-β** (blue). H atoms omitted for clarity; overlays generated in Mercury.

Chemical Science Accepted Manuscript

View Article Online
DOI: 10.1039/D6SC07012F

Open Access Article. Published on 24 June 2026. Downloaded on 6/25/2026 4:46:59 AM.
This article is licensed under a Creative Commons Attribution-NonCommercial 3.0 Unported Licence.

flipping of all three benzene rings around the central imine linkages, leading to a molecular conformational change and a total ~21% volume reduction relative to **2-tBP**. In contrast, **2-tBP-β** maintains a straight molecular conformation similar to the solvated structure, but rearranges its packing into a denser phase, resulting in a greater ~28% volume reduction relative to **2-tBP**.

As illustrated by the molecular overlay in Figure 5b and the dihedral angle data in Table S11 and S16-S18, the structural transformations among **2-tBP-acetone**, **2-tBP-α**, and **2-tBP-β** clearly reflect differing degrees of molecular flipping. Compared to the as-synthesized **2-tBP**, all three structures exhibit changes in the key dihedral angles Φ_{1-2}, Φ_{1-3}, and Φ_{1-4}. Notably, Φ_{1-3} associated with the central benzene ring and the most indicative of hinge-like motion in L2 increases from approximately 8° in **2-tBP** to 38° in **2-tBP-α**. In contrast, Φ_{1-3} in **2-tBP-β** changes relatively small, with values of 15° and 16° for L1 and L2, respectively, compared to 11° and 8° in **2-tBP**, respectively.

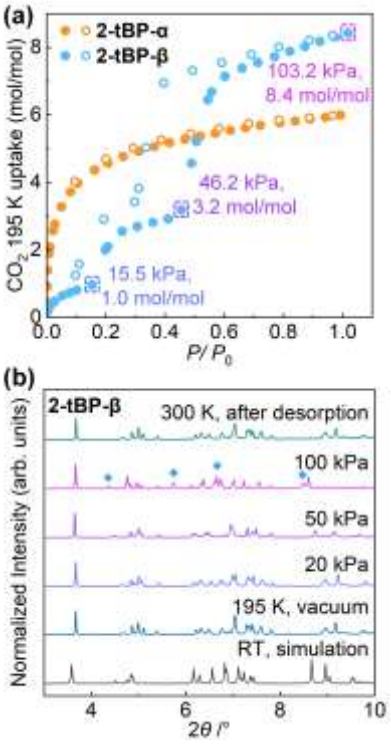

Figure 6. (a) CO_2 adsorption isotherms at 195 K for **2-tBP-α** (orange) and **2-tBP-β** (blue), key pressure points and stepped uptake associated with structural gating in **2-tBP-β** are highlighted. (b) In situ PXRD patterns (λ =0.9994128 Å) of **2-tBP-β** collected at 195 K under vacuum, at CO_2 pressures of 20, 50, and 100 kPa, and after desorption, together with the RT simulated pattern. The blue diamond symbols highlight the most pronounced new reflections associated with the open phase.

As shown in Figure S43a, the N_2 sorption isotherms at 77 K display very low uptake for both **2-tBP-α** and **2-tBP-β**, indicating that neither phase is accessible to N_2. This is consistent with the narrow channel window (Figure S51) diameters (2.32 Å for **2-tBP-α** and 2.01 Å for **2-tBP-β**) as calculated by Zeo++ for both static structures, which limit accessibility for N_2 (kinetic diameter, Dk = 3.64 Å) and even CO_2 (Dk = 3.30 Å).[37]

The CO_2 sorption isotherm at 195 K presents more prominent adsorption features (Figure 6a). The CO_2 adsorption isotherm of **2-tBP-β**, which has a smaller pore aperture and an extremely narrow channel (maximum pore diameter = 2.80 Å), displays a pronounced multi-step adsorption profile with distinct uptakes at approximately 15.5 and 46.2 kPa and a similar multi-step desorption with hysteresis. This multi-step behaviour with hysteresis suggests a sorption-induced structural rearrangement.[1, 38] This responsive behaviour was highly reproducible over at least three adsorption–desorption cycles, indicating the structural stability of the **2-tBP-β** during gas-induced transformations (Figure S43b). In addition, the crystalline phase remained intact after adsorption–desorption cycling and three days of water immersion at RT, indicating good structural stability (Figure S36a).

In contrast, **2-tBP-α**, with a larger pore maximum (5.43 Å) but narrow channel windows (2.32 Å), displays a type I adsorption isotherm without noticeable hysteresis or stepwise uptake (Figure 6a), demonstrating that its intrinsic local flexibility allows CO_2 to diffuse through the channel without significant rearrangement of the molecular conformation and packing.[39]

To better understand the distinct CO_2 adsorption behaviours of **2-tBP-α** and **2-tBP-β**, we performed *in situ* PXRD experiments under controlled CO_2 pressure. For **2-tBP-α**, no significant structural changes were observed upon CO_2 loading (Figure S37), consistent with its type I adsorption isotherm. The PXRD data of **2-tBP-β** shown in Figure 6b display clear and reversible structural transformations upon CO_2 loading (vacuum, 20, 50, 100 kPa and vacuum after testing). The contour plot of *in situ* PXRD intensity shown in Figure 7a illustrates the structural response of **2-tBP-β** to CO_2 adsorption at 195 K as a function of gas pressure. Notably, the contour plot shows that initial structural changes from the activated phase to the intermediate phase are minor, because the diffractions neither largely shift nor newly appear until 20 kPa. The large structural change occurred over 50 kPa from the intermediate to fully loaded phases to maximize the CO_2 capacity. This result suggests that the structure undergoes sequential reorganization as CO_2 pressure increases, rather than an abrupt switching between closed and open phases. Moreover, a prominent PXRD peak at $2\vartheta \approx 3.7°$ for **2-tBP-β**, assigned to the 001 reflection, remains at a constant position throughout the entire pressure range, indicating that the periodicity along the *c*-axis is largely retained during CO_2 adsorption. These results imply that the structural changes upon CO_2 adsorption mainly occur within the *ab* plane, possibly involving interlayer shifting or molecular flipping.

To further explore this scenario, we performed DFT optimizations to gain molecular-level insight into the guest-responsive behaviour of **2-tBP-β** (Figure 7b). First, we performed DFT energy calculations for the discrete RhMOC molecules in the gas phase, each in the conformations observed in the crystal structures. DFT computed energies revealed that the flipped conformation, found in **2-tBP-α**, is more thermodynamically stable (8.58 kJ/mol per cage) than the straight conformation of **2-tBP-β**. Interestingly, this thermodynamic stability is reversed in the crystalline phase. The DFT geometry optimized packing phase of **2-tBP-β** (named **2-**

Chemical Science Accepted Manuscript

 This journal is © The Royal Society of Chemistry 20xx

View Article Online
DOI: 10.1039/D6SC07013B

tBP-β-opt) is more thermodynamically stable (82.0 kJ/mol) than that of **2-tBP-α** (named **2-tBP-α-opt**). These calculations suggest that the straight conformation is more suitable to maximize the intermolecular interaction between the RhMOCs, even though the conformation itself is energetically less favoured (in the gas phase).

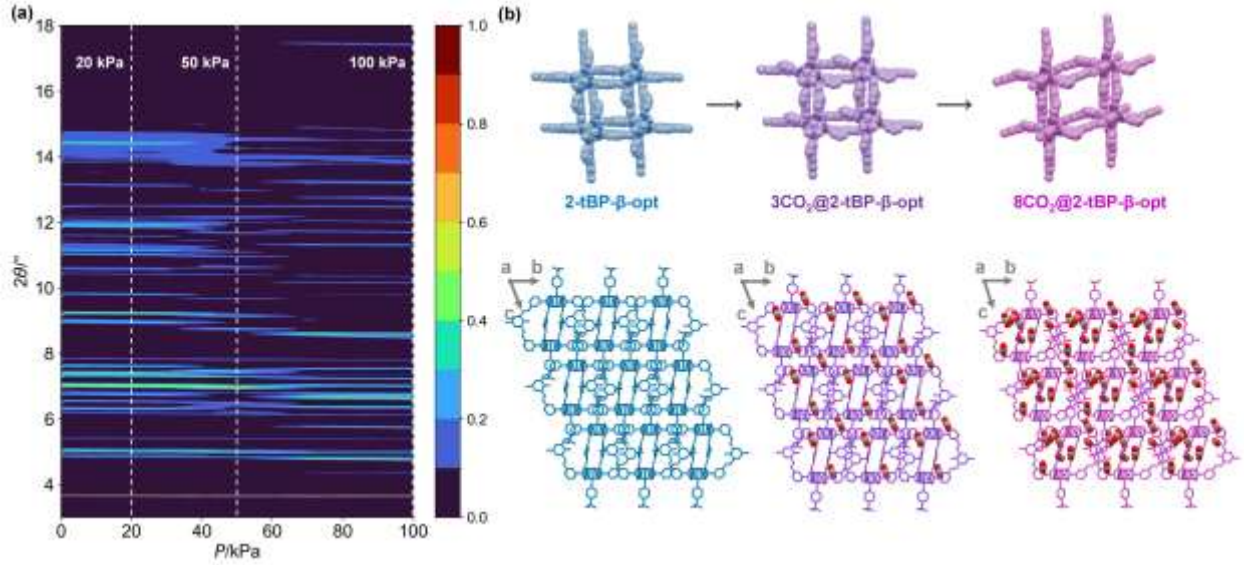

Figure 7. (a) Contour plot of *in situ* PXRD intensity (λ = 0.9994128 Å) for **2-tBP-β** over 2θ = 3–18° as a function of *P*. Dashed lines denote *P*= 20, 50, and 100 kPa. Intensities are normalized to the reflection at 2θ = 3.7°. (b) DFT-optimized packing of **2-tBP-β-opt** and CO_2-loaded open structure (**3CO_2@2-tBP-β-opt** and **8CO_2@2-tBP-β-opt**). H atoms omitted for clarity.

Next, we performed DFT optimizations on **2-tBP-β-opt** upon CO_2 loading. As shown in Table S7, CO_2 loading drives a progressive lattice expansion: the structure of **2-tBP-β-opt** loaded with three CO_2 molecules (**3CO_2@2-tBP-β-opt**) expands to 105%, increasing further to 121% when eight molecules are loaded (**8CO_2@2-tBP-β-opt**). This expansion arises mainly from molecular flipping and structural dislocation within the *ab* plane to accommodate CO_2, while the interlayer packing distance along the *c*-axis remains nearly unchanged (Figure 7b), consistent with the *in situ* PXRD results (Figure 7a).

According to the adsorbed CO_2 positions in **2-tBP-β-opt** shown in Figure S53, the adsorbed molecules are primarily located between the packing layers as observed in **1CO_2@2-tBP-β-opt** and **3CO_2@2-tBP-β-opt**. Upon further loading, CO_2 diffuses into the intrinsic cavity of RhMOC, accompanied by a greater degree of molecular flipping observed in **8CO_2@2-tBP-β-opt**. The calculated structure in Figure 7b and the detailed analysis of the dihedral angles around the imine linkages, summarized in Tables S19 and S21, reveal that the most pronounced conformational change occurs at Φ_{1-3}. For ligand L1, Φ_{1-3} increases markedly from 16° in **2-tBP-β-opt** to 28° in **8CO_2@2-tBP-β-opt**, while for L2 it rises from 12° to 21°. In comparison, the intermediate **3CO_2@2-tBP-β-opt** structure exhibits moderate Φ_{1-3} values of 20° for L1 and 16° for L2 (Table S20). These results further indicate the **2-tBP-β** progressively "opens its gate" through successive hinge-flipping motions and packing expansion as CO_2 pressure increases (Figure S53).

By comparison, the DFT-optimized structure of **2-tBP-α-opt**, featuring the initial flipped conformation, shows minimal structural and conformational changes even upon loading with 8 CO_2 molecules, consistent with the experimental gas sorption behavior and *in situ* PXRD results. (Table S6, Figure S37 and S52)

Conclusions

We reported a series of flexible dirhodium imine-functionalized MOCs, formed by a versatile covalent-linking approach. All six types of RhMOCs crystallize readily at ambient conditions and retain crystallinity upon activation. Systematic PXRD and gas sorption studies showed that tBP coordination at the axial site of RhMOC markedly improves the stability of molecular packing, which allows us to investigate the crystal structure after activation by 3D ED. Among these, the $ScCO_2$-activated **2-tBP-β** phase, possessing a metastable straight molecular conformation but the denser packing, exhibits repeatable CO_2-induced structural transformation. The combined *in situ* experiments with DFT calculations revealed that the flipping motion of the imine ligand and the molecular dislocation of MOCs are key to such structural flexibility. By contrast, the conventionally activated **2-tBP-α** phase, with a stable flipped conformation but less dense packing, exhibits a Type I isotherm and no structural transition, consistent with its larger cavity. Our studies demonstrate that the modular synthetic approach to generate a variety of flexible MOCs can deliver stable yet stimuli-responsive SPCs. Such phase-specific structural features give rise to distinct gas sorption behaviour, offering new design principles for adaptive materials in gas adsorption and separation.

Author contributions

D. H. and S. F. conceived and supervised the project. D. H. and J. L. C. designed and carried out the experiments and analysed the data. J. D. E. performed the DFT calculations. All authors

Open Access Article. Published on 24 June 2026. Downloaded on 6/25/2026 4:46:59 AM.
This article is licensed under a Creative Commons Attribution-NonCommercial 3.0 Unported Licence.
Chemical Science Accepted Manuscript

discussed the results and contributed to the writing of the manuscript.

Conflicts of interest

There are no conflicts to declare.

Data availability

The Supporting Information is available free of charge at XXX. CCDC 2488954-2488966 contains the supplementary crystallographic data for this paper. These data can be obtained free of charge via www.ccdc.cam.ac.uk/data_request/cif, or by emailing data_request@ccdc.cam.ac.uk, or by contacting the Cambridge Crystallographic Data Center, 12 Union Road, Cambridge CB12 1EZ UK; fax: +44 1223 336033. A supporting data repository containing simulation files is available at Zenodo: https://doi.org/10.5281/zenodo.17104742.

Acknowledgements

D.H. gratefully acknowledges the JSPS Postdoctoral Fellowship Program for Foreign Researchers. This work was supported by the Japan Society for the Promotion of Science (JSPS) KAKENHI (JP23H00298), the Japan Science and Technology Agency (JST) through the Adopting Sustainable Partnerships for Innovative Research Ecosystem (ASPIRE) program (JPMJAP2424), and the JSPS Postdoctoral Fellowship for Foreign Researchers (JP23KF0148). Synchrotron PXRD measurements were performed at SPring-8 with the approval of the Japan Synchrotron Radiation Research Institute (JASRI) at beamlines BL02B1 (Proposal 2025A1774) and BL02B2 (Proposals 2024A1907, 2024B1653 and 2025A1968). We also thank the iCeMS Analysis Centre for access to 3D ED (XtaLAB Synergy-ED). J.D.E. acknowledges support from the Australian Research Council through a Discovery Early Career Researcher Award (DE220100163). Computational resources were provided by the Phoenix HPC service at the University of Adelaide. This research was also supported by the Australian Government's National Collaborative Research Infrastructure Strategy (NCRIS), with access to computational resources provided by the Pawsey Supercomputing Research Centre through the National Computational Merit Allocation Scheme.

Notes and references

1 S. Krause, N. Hosono, S. Kitagawa, *Angew. Chem. Int. Ed.*, 2020, **59**, 15325–15341.
2 L. Vanduyfhuys, S. M. J. Rogge, J. Wieme, S. Vandenbrande, G. Maurin, M. Waroquier, V. Van Speybroeck, *Nat. Commun.*, 2018, **9**, 204.
3 S. Horike, S. Shimomura, S. Kitagawa, *Nat. Chem.*, 2009, **1**, 695–704.
4 M. Bonneau, C. Lavenn, J.-J. Zheng, A. Legrand, T. Ogawa, K. Sugimoto, F.-X. Coudert, R. Reau, S. Sakaki, K.-i. Otake, S. Kitagawa, *Nat. Chem.*, 2022, **14**, 816–822.
5 L. Bondorf, J. L. Fiorio, V. Bon, L. Zhang, M. Maliuta, S. Ehrling, I. Senkovska, J. D. Evans, J.-O. Joswig, S. Kaskel, T. Heine, M. Hirscher, *Sci. Adv.*, 2022, **8**, eabn7035.
6 H. Furukawa, K. E. Cordova, M. O'Keeffe, O. M. Yaghi, *Science*, 2013, **341**, 1230444.
7 J.-P. Zhang, H.-L. Zhou, D.-D. Zhou, P.-Q. Liao, X.-M. Chen, *Natl. Sci. Rev.*, 2017, **5**, 907–919.
8 P. Wang, K.-i. Otake, N. Hosono, S. Kitagawa, *Angew. Chem. Int. Ed.*, 2021, **60**, 7030–7035.
9 G.-A. Li, M. Deng, W. Guo, S. Yin, Y.-E. Liu, A.-X. Zhu, M. J. Zaworotko, *Inorg. Chem. Front.*, 2025, **12**, 3449–3455.
10 H. Wang, W. Zuo, Z. Wang, W. Jiang, S. Liu, T. Zeng, W. Lei, Z. Yin, M.-H. Zeng, Y.-B. Zhang, *Angew. Chem. Int. Ed.*, 2025, **64**, e202512425.
11 T. Tateishi, M. Yoshimura, S. Tokuda, F. Matsuda, D. Fujita, S. Furukawa, *Coord. Chem. Rev.*, 2022, **467**, 214612.
12 B. S. Pilgrim, N. R. Champness, *ChemPlusChem*, 2020, **85**, 1842–1856.
13 H. Dasary, R. Jagan, D. K. Chand, *Inorg. Chem.*, 2018, **57**, 12222–12231.
14 H. Xu, T. K. Ronson, A. W. Heard, P. C. P. Teeuwen, L. Schneider, P. Pracht, J. D. Thoburn, D. J. Wales, J. R. Nitschke, *Nat. Chem.*, 2025, **17**, 289–296.
15 T. Abe, K. Takeuchi, M. Higashi, H. Sato, S. Hiraoka, *Nat. Commun.*, 2024, **15**, 7630.
16 E. Benchimol, J. Tessarolo, G. H. Clever, *Nat. Chem.*, 2024, **16**, 13–21.
17 G. A. Craig, P. Larpent, S. Kusaka, R. Matsuda, S. Kitagawa, S. Furukawa, *Chem. Sci.*, 2018, **9**, 6463–6469.
18 G. A. Craig, P. Larpent, H. Urabe, A. Legrand, M. Bonneau, S. Kusaka, S. Furukawa, *Chem. Commun.*, 2020, **56**, 3689–3692.
19 B. Lee, B. Go, B. Jung, J. Park, *Small*, 2024, **20**, 2308393.
20 S. Delaporte, I. Abánades Lázaro, J. López-Cabrelles, E. C. Mazarakioti, S. Chebourou, I. J. Vitórica-Yrezábal, M. Giménez-Marqués, G. Mínguez Espallargas, *Dalton Trans.*, 2023, **52**, 15682–15687.
21 M. Zhou, G. Liu, Z. Ju, K. Su, S. Du, Y. Tan, D. Yuan, *Cryst. Growth Des.*, 2020, **20**, 4127–4134.
22 S. Lee, H. Jeong, D. Nam, M. S. Lah, W. Choe, *Chem. Soc. Rev.*, 2021, **50**, 528–555.
23 J. Martí-Rujas, *Commun. Chem.*, 2025, **8**, 92.
24 T. Hasell, A. I. Cooper, *Nat. Rev. Mater.*, 2016, **1**, 16053.
25 J. Albalad, A. Carné-Sánchez, T. Grancha, L. Hernández-López, D. Maspoch, *Chem. Commun.*, 2019, **55**, 12785–12788.
26 C. Itoh, M. Kitada, M. Kondo, S. Masaoka, H. Yoshino, W. Kosaka, Y. Ootani, J. Matsuda, M. Kubo, T. J. Konno, H. Miyasaka, *ChemSusChem*, 2024, **17**, e202400885.
27 A. M. Dennis, R. A. Howard, J. L. Bear, J. D. Korp, I. Bernal, *Inorg. Chim. Acta*, 1979, **37**, L561–L563.
28 F. Mu, S. L. Coffing, D. J. Riese, R. L. Geahlen, P. Verdier-Pinard, E. Hamel, J. Johnson, M. Cushman, *J. Med. Chem.*, 2001, **44**, 441–452.
29 S. Furukawa, N. Horike, M. Kondo, Y. Hijikata, A. Carné-Sánchez, P. Larpent, N. Louvain, S. Diring, H. Sato, R. Matsuda, R. Kawano, S. Kitagawa, *Inorg. Chem.*, 2016, **55**, 10843–10846.
30 A. W. Markwell-Heys, M. L. Schneider, J. M. L. Madridejos, G. F. Metha, W. M. Bloch, *Chem. Commun.*, 2021, **57**, 2915–2918.
31 T. Steiner, *Angew. Chem. Int. Ed.*, 2002, **41**, 48–76.
32 J. E. Mondloch, O. Karagiaridi, O. K. Farha, J. T. Hupp, *CrystEngComm*, 2013, **15**, 9258–9264.
33 D. He, H. Ji, T. Liu, M. Yang, R. Clowes, M. A. Little, M. Liu, A. I. Cooper, *J. Am. Chem. Soc.*, 2024, **146**, 17438–17445.
34 W. M. Bloch, R. Babarao, M. L. Schneider, *Chem. Sci.*, 2020, **11**, 3664–3671.
35 J. W. M. Osterrieth, J. Rampersad, D. Madden, N. Rampal, L. Skoric, B. Connolly, M. D. Allendorf, V. Stavila, J. L. Snider, R. Ameloot, J. Marreiros, C. Ania, D. Azevedo, E. Vilarrasa-Garcia,

View Article Online DOI: 10.1039/D5SC05012B

Open Access Article. Published on 24 June 2026. Downloaded on 6/25/2026 4:46:59 AM. This article is licensed under a Creative Commons Attribution-NonCommercial 3.0 Unported Licence.

Chemical Science Accepted Manuscript

This journal is © The Royal Society of Chemistry 20xx

View Article Online
DOI: 10.1039/D6SC03012B

B. F. Santos, X.-H. Bu, Z. Chang, H. Bunzen, N. R. Champness, S. L. Griffin, B. Chen, R.-B. Lin, B. Coasne, S. Cohen, J. C. Moreton, Y. J. Colón, L. Chen, R. Clowes, F.-X. Coudert, Y. Cui, B. Hou, D. M. D'Alessandro, P. W. Doheny, M. Dincă, C. Sun, C. Doonan, M. T. Huxley, J. D. Evans, P. Falcaro, R. Ricco, O. Farha, K. B. Idrees, T. Islamoglu, P. Feng, H. Yang, R. S. Forgan, D. Bara, S. Furukawa, E. Sanchez, J. Gascon, S. Telalović, S. K. Ghosh, S. Mukherjee, M. R. Hill, M. M. Sadiq, P. Horcajada, P. Salcedo-Abraira, K. Kaneko, R. Kukobat, J. Kenvin, S. Keskin, S. Kitagawa, K.-I. Otake, R. P. Lively, S. J. A. DeWitt, P. Llewellyn, B. V. Lotsch, S. T. Emmerling, A. M. Pütz, C. Martí-Gastaldo, N. M. Padial, J. García-Martínez, N. Linares, D. Maspoch, J. A. Suárez Del Pino, P. Moghadam, R. Oktavian, R. E. Morris, P. S. Wheatley, J. Navarro, C. Petit, D. Danaci, M. J. Rosseinsky, A. P. Katsoulidis, M. Schröder, X. Han, S. Yang, C. Serre, G. Mouchaham, D. S. Sholl, R. Thyagarajan, D. Siderius, R. Q. Snurr, R. B. Goncalves, S. Telfer, S. J. Lee, V. P. Ting, J. L. Rowlandson, T. Uemura, T. Iiyuka, M. A. van der Veen, D. Rega, V. Van Speybroeck, S. M. J. Rogge, A. Lamaire, K. S. Walton, L. W. Bingel, S. Wuttke, J. Andreo, O. Yaghi, B. Zhang, C. T. Yavuz, T. S. Nguyen, F. Zamora, C. Montoro, H. Zhou, A. Kirchon, D. Fairen-Jimenez, *Adv. Mater.*, 2022, **34**, e2201502.

36 T. F. Willems, C. H. Rycroft, M. Kazi, J. C. Meza, M. Haranczyk, *Microporous Mesoporous Mater.*, 2012, **149**, 134–141.

37 M. P. Snelgrove, B. Doñagueda Suso, C. S. Sangster, K. Asif, E. Regincós Martí, D. J. Ashworth, J. P. Tidey, J. R. B. Gomes, M. Jorge, A. R. Kennedy, S. Parsons, A. J. Fletcher, G. A. Craig, *Angew. Chem. Int. Ed.*, 2025, **64**, e202514527.

38 J. D. Evans, V. Bon, I. Senkovska, H.-C. Lee, S. Kaskel, *Nat. Commun.*, 2020, **11**, 2690.

39 D. Fairen-Jimenez, S. A. Moggach, M. T. Wharmby, P. A. Wright, S. Parsons, T. Düren, *J. Am. Chem. Soc.*, 2011, **133**, 8900–8902.

Open Access Article. Published on 24 June 2026. Downloaded on 6/25/2026 4:46:59 AM.
This article is licensed under a Creative Commons Attribution-NonCommercial 3.0 Unported Licence.

Chemical Science Accepted Manuscript

View Article Online
DOI: 10.1039/D6SC03012B

The Supporting Information is available free of charge at XXX. CCDC 2488954-2488966 contains the supplementary crystallographic data for this paper. These data can be obtained free of charge via www.ccdc.cam.ac.uk/data_request/cif, or by emailing data_request@ccdc.cam.ac.uk, or by contacting the Cambridge Crystallographic Data Center, 12 Union Road, Cambridge CB12 1EZ UK; fax: +44 1223 336033.

A supporting data repository containing simulation files is available at Zenodo: https://doi.org/10.5281/zenodo.17104742.

Open Access Article. Published on 24 June 2026. Downloaded on 6/25/2026 4:46:59 AM.
This article is licensed under a Creative Commons Attribution-NonCommercial 3.0 Unported Licence.

Chemical Science Accepted Manuscript